NEOPLASIA
www.neoplasia.com

Volume 10 Number 4 April 2008 pp. 354–362 354

Tumor Vascularity Assessed By Magnetic Resonance Imaging and Intravital Microscopy Imaging[1]

Jon-Vidar Gaustad*, Kjetil G. Brurberg*, Trude G. Simonsen*, Camilla S. Mollatt* and Einar K. Rofstad*

*Group of Radiation Biology and Tumor Physiology, Department of Radiation Biology, Institute for Cancer Research, Norwegian Radium Hospital, Montebello, Oslo, Norway

Abstract

Gadopentetate dimeglumine (Gd-DTPA)–based dynamic contrast-enhanced magnetic resonance imaging (DCE-MRI) is considered to be a useful method for characterizing the vascularity of tumors. However, detailed studies of experimental tumors comparing DCE-MRI–derived parametric images with images of the morphology and function of the microvascular network have not been reported. In this communication, we describe a novel MR-compatible mouse dorsal window chamber and report comparative DCE-MRI and intravital microscopy studies of A-07-GFP tumors xenografted to BALB/c *nu/nu* mice. Blood supply time (BST) images (i.e., images of the time from when arterial blood enters a tumor through the supplying artery until it reaches a vessel segment within the tumor) and morphologic images of the microvascular network were produced by intravital microscopy. Images of $E{\cdot}F$ (E is the initial extraction fraction of Gd-DTPA and F is perfusion) were produced by subjecting DCE-MRI series to Kety analysis. The $E{\cdot}F$ images mirrored the morphology (microvascular density) and the function (BST) of the microvascular networks well. Tumor regions showing high $E{\cdot}F$ values colocalized with tumor regions showing high microvascular density and low BST values. Significant correlations were found between $E{\cdot}F$ and microvascular density and between $E{\cdot}F$ and BST, both within and among tumors.

Neoplasia (2008) 10, 354–362

Introduction

Human and experimental tumors develop a highly heterogeneous physiological microenvironment during growth characterized by oxygen and nutrient depletion, low energy status, extracellular acidosis, and interstitial hypertension [1]. This hostile microenvironment causes resistance to treatment and may promote malignant progression, invasive growth, and metastatic dissemination [2,3]. The physiological parameters of the tumor microenvironment are determined primarily by the blood perfusion, which is inadequate and heterogeneous in most tumors, primarily because of severe structural and architectural abnormalities in the microvascular network [1–4].

It has been suggested that gadopentetate dimeglumine (Gd-DTPA)–based dynamic contrast-enhanced magnetic resonance imaging (DCE-MRI) may be a useful noninvasive diagnostic method for characterizing the vascularity of tumors. The uptake of Gd-DTPA in tumor tissue depends on several vascular and nonvascular parameters, including blood perfusion, microvascular density, vessel wall permeability, cell density, extracellular volume fraction, and extracellular matrix density [5]. A variety of qualitative, semiquantitative, and quantitative strategies are being used for analyzing DCE-MRI series of tumors [6]. The most promising quantitative methods are based on the use of pharmacokinetic models of the uptake of Gd-DTPA in the tumor tissue [6,7]. However, the parameters derived from these models describe the kinetics of Gd-DTPA distribution rather than true tumor physiology and are thus only surrogate parameters for physiological parameters.

Abbreviations: BST, blood supply time; DCE-MRI, dynamic contrast-enhanced magnetic resonance imaging; $E{\cdot}F$, extraction-perfusion product, where E is the initial extraction fraction of Gd-DTPA and F is blood perfusion; Gd-DTPA, gadopentetate dimeglumine; GFP, green fluorescence protein; K^{trans}, volume transfer constant of Gd-DTPA; ROI, region of interest; TRITC, tetramethylrhodamine isothiocyanate; v_e, distribution volume of Gd-DTPA per unit volume of tissue; λ, partition coefficient of Gd-DTPA

Address all correspondence to: Einar K. Rofstad, PhD, Department of Radiation Biology, Institute for Cancer Research, Norwegian Radium Hospital, Montebello, N-0310 Oslo, Norway. E-mail: einar.k.rofstad@rr-research.no

[1]This work was supported by the Norwegian Cancer Society.
Received 14 January 2008; Revised 6 February 2008; Accepted 6 February 2008

DOI 10.1593/neo.08162

It is thus generally accepted that the validity of the DCE-MRI–derived parameters and parametric images used for characterizing the physiological microenvironment of tumors needs to be evaluated carefully [6,7].

A commonly used evaluation strategy is to compare DCE-MRI–derived parameters with histologic parameters of the imaged tumors [8–13]. Thus, correlations have been found between DCE-MRI–derived parameters and microvascular density in breast carcinoma [8], cervical carcinoma [9], and cerebral glioma [10]. Moreover, DCE-MRI–derived parameters have been shown to correlate with the expression of vascular endothelial growth factor-A in breast carcinoma [11,12] and colorectal carcinoma [13]. However, the correlations were, in general, weak possibly because the DCE-MRI–derived parameters used in these studies were not adequate measures of tumor vascularity or because the biopsies used for preparation of histologic sections were not representative for the imaged tissue.

The potential usefulness of Gd-DTPA–based DCE-MRI in characterizing the microenvironment of tumors is currently being evaluated in our laboratory by using human tumor xenografts as preclinical models of human cancer [14–17]. Our studies have shown that highly reproducible images of $E{\cdot}F$ (E is the initial extraction fraction of Gd-DTPA and F is blood perfusion) and λ (λ is proportional to extracellular volume fraction) can be obtained by subjecting DCE-MRI series to Kety analysis [14,15]. We have also performed experiments showing that $E{\cdot}F$ may be correlated to microvascular density and fraction of radiobiologically hypoxic cells in human melanoma xenografts [16,17]. These experiments provided significant evidence that DCE-MRI may be a useful imaging method for characterizing the microenvironment of tumors. However, because microvascular density is a global parameter and measurement of fraction of radiobiologically hypoxic cells requires tumor disaggregation, our studies did not allow a direct comparison of $E{\cdot}F$ images and images of the tumor microenvironment.

Detailed studies of the microenvironment of tumors can be performed by the use of window chamber preparations and intravital microscopy techniques [18–22]. These methods are particularly useful for providing high-resolution images of the morphology and function of tumor microvascular networks. DCE-MRI studies of tumors growing in window chamber preparations have not been reported thus far, probably because MR-compatible window chambers are not available. An MR-compatible mouse dorsal window chamber was recently constructed by the Group of Radiation Biology and Tumor Physiology at the Norwegian Radium Hospital. In the present communication, we describe this window chamber and report comprehensive studies comparing DCE-MRI–derived $E{\cdot}F$ images with optical images of tumor vascularity. The main purpose of the work was to investigate to what extent $E{\cdot}F$ images reflect morphologic and functional images of the microvascular network of tumors. The morphologic parameters used in our work included vessel length density, vascular area fraction, and interstitial distance, whereas blood supply time [BST (i.e., the time required for arterial blood to flow from the main tumor-supplying artery to a downstream tumor microvessel segment)] [23] was used as functional parameter.

Materials and Methods

Mice

Adult (8–10 weeks of age) female BALB/c *nu/nu* mice, bred and maintained as described elsewhere [23], were used as host animals for dorsal window chamber preparations. The animal experiments were approved by the Institutional Committee on Research Animal Care and were done according to the Interdisciplinary Principles and Guidelines for the Use of Animals in Research, Marketing, and Education (New York Academy of Sciences, New York, NY).

Cells and Multicellular Spheroids

A-07 human melanoma cells [24] were constitutively transfected with green fluorescence protein (GFP) by lipofection. The transfected cells (A-07-GFP) were grown as monolayers in RPMI 1640 (25 mM HEPES and l-glutamine) supplemented with 13% bovine calf serum, 700 μg/ml genetecin, 250 μg/ml penicillin, and 50 μg/ml streptomycin. Multicellular spheroids of A-07-GFP cells were produced and maintained by using a liquid-overlay culture technique [25]. Monolayer cultures and spheroids were incubated at 37°C in a humidified atmosphere of 5% CO_2 in air and subcultured twice a week.

Anesthesia

Window chamber implantation, intravital microscopy, and DCE-MRI were carried out with anesthetized mice. Fentanyl citrate (Janssen Pharmaceutica, Beerse, Belgium), fluanisone (Janssen Pharmaceutica), and midazolam (Hoffmann-La Roche, Basel, Switzerland) were administered i.p. in doses of 0.63, 20, and 10 mg/kg, respectively.

Window Chamber Preparations

Window chambers were implanted into the dorsal skin fold of mice by using a procedure similar to that described by Papenfuss et al. [26]. Briefly, the chamber consisted of parallel frames, and after implantation, these frames sandwiched an extended double layer of skin (Figure 1). Before the chamber was implanted, a circular hole with a diameter of ~6.0 mm was made in one of the skin layers. A plastic window with a diameter of 6.0 mm was attached to the frame on the surgical side with a clip to provide visual access to the fascial side of the opposite skin layer. The frames and the clip were in-house-made of polymer material (Victrex PEEK; Victrex Technology Centre, Thornton Cleveleys, UK). The composite chamber had a total weight of 1.0 g. Tumors were initiated by implanting an A-07-GFP spheroid with a diameter of 100 to 200 μm onto the fascial side of the intact skin layer. After surgery, the mice were given buprenorphine (Temgesic; Schering-Plough, Brussels, Belgium) i.p. in a dose of 0.12 mg/kg.

Intravital Microscopy

Tumor vascular morphology and blood flow were imaged by using an inverted fluorescence microscope equipped with filters for green and red lights (IX-71; Olympus, Munich, Germany), a black and white CCD camera (C4742-95; Hamamatsu Photonics, Hamamatsu, Japan), and appropriate image acquisition software (Wasabi; Hamamatsu Photonics). Tetramethylrhodamine isothiocyanate dextran (TRITC-dextran) with a molecular weight of 155 kDa (Sigma Aldrich, St. Louis, MO) was used as vascular tracer. A 0.2-ml bolus of TRITC-dextran (50 mg/ml) was injected into the lateral tail vein, and first-pass imaging movies were recorded at a frame rate of 18 frames per second (fps) by using a ×1.25 objective lens, resulting in a time resolution of 55.6 milliseconds, a field of view of 6.89 × 5.51 mm^2, and a pixel size of 10.8 × 10.8 μm^2. Afterwards, the entire vasculature network was mapped by recording 9 to 16 single frames with a ×4 objective lens, resulting in a field of view of 2.15 × 1.72 mm^2 and a pixel size of 3.4 × 3.4 μm^2. During imaging, the mice were kept

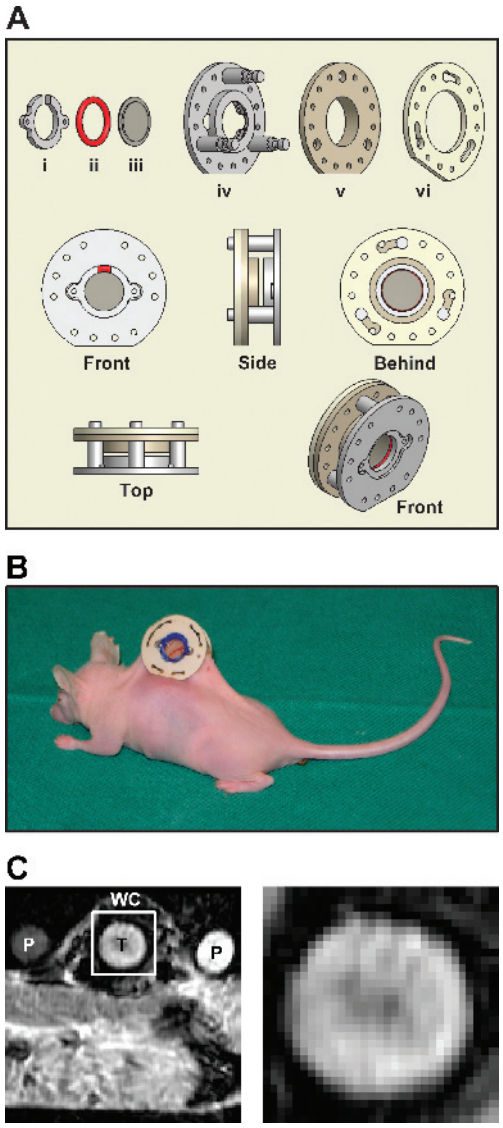

Figure 1. (A) Technical drawing of our MR-compatible mouse dorsal window chamber. The chamber consists of a clip (i), a silicon ring (ii), a transparent plastic window with a diameter of 6.0 mm (iii), and three frames (iv–vi). The frames and the clip were in-house-made of polymer material (Victrex PEEK; Victrex Technology Centre). The chamber has an outer diameter of 19.0 mm, an outer thickness of 7.0 mm, and a total weight of 1.0 g. (B) Photograph of the MR-compatible chamber implanted in the dorsal skin fold of a BALB/c *nu/nu* mouse. The tumor vasculature is visible through the transparent window. (C) A low-magnification gradient echo image showing the calibration phantoms (P) and a mouse bearing a window chamber (WC) with an A-07-GFP tumor (T) (left) and a high-magnification image of the outlined region, showing the tumor (right).

in a specially constructed holder that fixed the window chamber to the microscope stage. The body core temperature of the mice was kept at 37 to 38°C by using a hot-air generator. The recordings were stored and analyzed offline. Tumor size (i.e., tumor area) was calculated from the number of pixels showing GFP fluorescence.

Vascular Masks and BST Images

Two-dimensional projected vascular masks were established from stored images by using an in-house-made computer program. The algorithms used for identification of microvascular networks were implemented in MATLAB software (The MathWorks, Natick, MA). Background heterogeneities were removed by using a white top hat transformation. The images were eroded by linear structure elements, and local thresholding was carried out. Finally, the images were cleaned up by applying scrapping and hole filling procedures. Vascular masks established from high-resolution images (i.e., images recorded by a ×4 objective lens) were used to compute morphologic parameters. The following morphologic parameters were computed: total vessel length per μm^2 tumor area, length of large vessels (i.e., vessels with diameter ≥23.8 μm, corresponding to 7 pixels) per μm^2 tumor area, vascular area fraction [i.e., # pixels (vascular mask)/# pixels (tumor)], and interstitial distance (i.e., the median of the distance from a tumor pixel outside the vascular mask to the nearest pixel within the vascular mask). Blood supply time images were produced by assigning a BST value to each pixel of the vascular masks. The BST of a pixel was measured as the time difference between the frame showing maximum fluorescence intensity in the pixel and the frame showing maximum fluorescence intensity in the main tumor-supplying artery, as described in detail previously [23].

Dynamic Contrast-Enhanced Magnetic Resonance Imaging

DCE-MRI was performed by using a procedure similar to that described in great detail elsewhere [17]. Briefly, a 1.5-T whole-body scanner (Signa; General Electric, Milwaukee, WI) and a cylindrical slotted tube resonator transceiver coil especially constructed for mice [27] were used for imaging. The tumors were imaged sagittally in a single scan adjacent to and parallel to the window of the chamber preparations at a voxel size of 0.31 × 0.31 × 2.0 mm^3 and with a time resolution of 14 seconds. The sequences of the DCE-MRI sessions have been described previously [17]. Tumor size (i.e., tumor area) was calculated from the number of pixels showing Gd-DTPA–induced contrast enhancement in T_1-weighted images.

Analysis of DCE-MRI Data

The DCE-MRI series were subjected to Kety analysis as described in detail previously [14–17]. Briefly, Gd-DTPA concentrations were calculated from signal intensities by using the method of Hittmair et al. [28]. Plots of Gd-DTPA concentration *versus* time were generated, and the Kety equation [29],

$$C_t(T) = E \cdot F \cdot \int_0^T C_a(t) \cdot e^{-E \cdot F \cdot (T-t)/\lambda} dt,$$

was fitted to the plots, where $C_t(T)$ is the Gd-DTPA concentration in the tumor tissue at time T, E is the initial extraction fraction of Gd-DTPA, F is the perfusion per unit tumor volume, $C_a(t)$ is the arterial input function, and λ represents the partition coefficient of Gd-DTPA and is proportional to the extracellular volume fraction. The arterial input function was determined as described elsewhere [14,30]. Numerical values of $E \cdot F$ [in ml/g per minute] and λ were determined for each voxel from the best curve fit. The uncertainty in the assessment of $E \cdot F$ and λ was investigated by subjecting the DCE-MRI data to Monte Carlo analysis, using noise generated from the residuals of the Kety curve fits [30]. The standard deviation of $E \cdot F$ was found to be less than 0.005 ml/g per minute for all values of $E \cdot F$, whereas λ showed a standard deviation that increased from 0.007 to 0.012 with increasing $E \cdot F$ value.

Statistical Analysis

Correlations between two parameters were searched for by linear regression analysis. Probability values (P) and correlation coefficients (R) were calculated by using the SigmaStat statistical software (SPSS Science, Chicago, IL). A significance criterion of $P < .05$ was used.

Results

An MR-compatible mouse dorsal window chamber was constructed and produced (Figure 1*A*), and eleven A-07-GFP tumors were transplanted to the chamber and examined. The tumors grew as a hemisphere in the chamber, with the plane surface facing the window (Figure 1*B*). When the area of this surface had grown to a size of 10 to 30 mm^2, a bolus of TRITC-dextran was administered i.v., and a first-pass imaging movie of the entire tumor surface was recorded before the microvascular network was mapped at a higher magnification. The tumors were subjected to DCE-MRI ~6 hours later. The chamber did not induce artifacts in the MR images of the tumors (Figure 1*C*).

The tumors differed substantially in vascularity. This is illustrated in Figure 2, which shows the intravital microscopy image of the microvascular network, the DCE-MRI–derived *E·F* image, and the *E·F* frequency distribution of a homogeneous and well-vascularized tumor (Figure 2*A*) and a heterogeneous and poorly vascularized tumor (Figure 2*B*).

To compute morphologic parameters from microvascular network images, vascular masks were made from the images (i.e., pixels within and outside the network were given the values 1 and 0, respectively). The general quality of the masks is illustrated in Figure 3, which shows low- and high-magnification images of a microvascular network (Figure 3*A*), low- and high-magnification binary images of the corresponding vascular mask (Figure 3*B*), and low- and high-magnification images of the contour of the vascular mask superimposed on low- and high-magnification images of the microvascular network (Figure 3*C*).

Quantitative analysis of the vascular masks showed that the microvascular density differed substantially among the eleven tumors. Thus, total vessel length per unit tumor area ranged from 0.013 to 0.025 per μm with a mean value of 0.018 per μm, length of large vessels per unit tumor area ranged from 0.0080 to 0.0099 per μm with a mean value of 0.0091 per μm, vascular area fraction ranged from 0.36 to 0.42 with a mean value of 0.39, and interstitial distance ranged from 10.6 to 21.5 μm with a mean value of 15.5 μm. In comparison, median *E·F* of the tumors ranged from 0.40 to 1.31 ml/g per minute with a mean value of 0.76 ml/g per minute.

A detailed comparison of intravital microscopy images and DCE-MRI–derived images requires that the tumor size is identical in the two types of images. There was a nearly one-to-one correlation between the tumor area determined from the GFP-signal in the intravital microscopy experiments and the tumor area determined from the Gd-DTPA–induced contrast enhancement in the DCE-MRI experiments. This is illustrated in Figure 4*A*, which shows tumor area measured by DCE-MRI *versus* tumor area measured by intravital microscopy ($R^2 = 0.91$; $P = .000006$).

Correlations between *E·F* and morphologic parameters of the microvasculature were searched for at three levels: by calculating numerical values of *E·F* and morphologic parameters for whole tumors, for three concentric circular regions of interest (ROIs), and for quadratic ROIs corresponding to 4 × 4 *E·F* pixels. The morphologic images and the *E·F* images were divided into circular and quadratic ROIs as illustrated in Figure 4*B* (*left* and *right*, respectively). The tumor used as example showed radial heterogeneity in *E·F* and microvascular density. Both *E·F* and vascular area fraction were highest in the peripheral ROI, second highest in the middle ROI, and lowest in the central ROI (Figure 4*B*, *left*). Moreover, there was a significant correlation between *E·F* and vascular area fraction for the quadratic

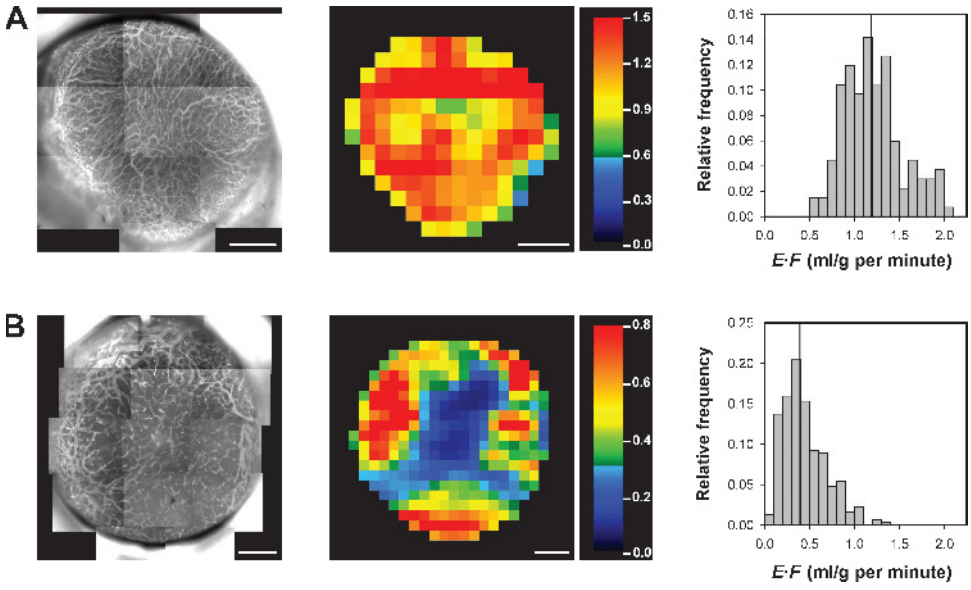

Figure 2. Intravital microscopy images of the microvascular network (left panels), DCE-MRI–derived *E·F* images (middle panels), and the corresponding *E·F* frequency distributions (right panels) of a homogeneous and well-vascularized A-07-GFP tumor (A) and a heterogeneous and poorly vascularized A-07-GFP tumor (B). The color bars show the *E·F* scales. The vertical lines in the *E·F* frequency distributions indicate median *E·F*. Scale bars, 1 mm.

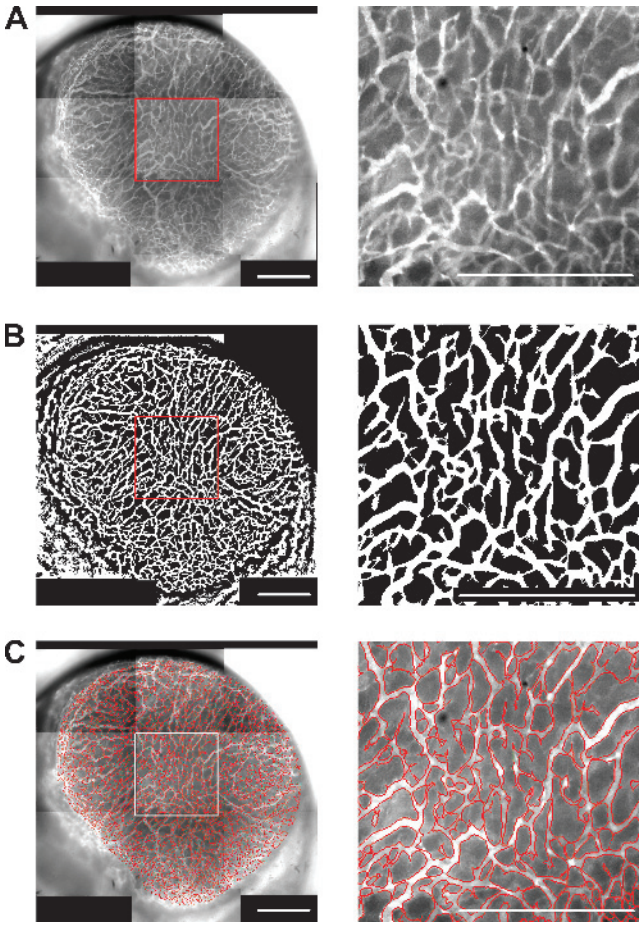

Figure 3. Intravital microscopy images of the microvascular network (A), binary images of the corresponding vascular mask (B), and images showing the contour of the vascular mask superimposed on the microvascular network (C) of a homogeneous and well-vascularized A-07-GFP tumor. The panels to the left refer to the entire microvascular network of the tumor. The panels to the right show high-magnification images of the outlined region. Scale bars, 1 mm.

ROIs (Figure 4*B*, *right*; R^2 = 0.35; P = .016). Similar correlations were found for all heterogeneous tumors. Thus, when the quadratic ROIs differed significantly in *E·F* (i.e., when the differences in *E·F* among the ROIs were large compared with the experimental uncertainty in *E·F*), *E·F* increased significantly with increasing microvascular density. However, for homogeneous tumors (i.e., when the differences in *E·F* among the quadratic ROIs were similar to the experimental uncertainty in *E·F*), significant correlations between *E·F* and one or more of the morphologic parameters could not be detected.

The data for all 11 tumors are summarized in Figure 4*C*. With only two exceptions, significant correlations were found between *E·F* and microvascular density, regardless of whether the analysis was based on whole tumors (*left column*), circular ROIs (*middle column*), or quadratic ROIs (*right column*), and regardless of whether total vessel length per μm^2 tumor area (*first row*), length of large vessels per μm^2 tumor area (*second row*), vascular area fraction (*third row*), or interstitial distance (*fourth row*) was used as parameter for microvascular density. The exceptions were *E·F versus* total vessel length per μm^2 tumor area (whole tumors) and *E·F versus* interstitial distance (whole tumors). The strongest correlations were found when microvascular density was measured as length of large vessels per μm^2 tumor area [R^2 = 0.81, P = .00014 (whole tumors); R^2 = 0.56, P < .000001 (circular ROIs); R^2 = 0.39, P < .000001 (quadratic ROIs)]. There was no correlation between *E·F* and vessel diameter (P > .05) or between *E·F* and tumor size (P > .05).

Moreover, *E·F* was inversely correlated to BST. This is illustrated qualitatively in Figure 5, which shows single frames from the first-pass imaging movie, the *E·F* image, and the *E·F* frequency distribution of a well-vascularized (Figure 5*A*) and a poorly vascularized (Figure 5*B*) tumor. The entire microvascular network of the well-vascularized tumor was filled with TRITC-dextran 1.3 seconds after the bolus had reached the main tumor-supplying artery, and the *E·F* values were high in all regions of the tumor. In the poorly vascularized tumor, on the other hand, a large central region of the microvascular network was not filled with TRITC-dextran even 5 seconds after the bolus had reached the main tumor-supplying artery, and this region of the tumor showed low *E·F* values.

The correlation between *E·F* and BST is illustrated quantitatively in Figure 6 by using a heterogeneously vascularized tumor as example. The figure shows two single frames from the first-pass imaging movie of the tumor and curves for relative signal intensity *versus* time for the ROIs indicated in the frames (Figure 6*A*), the BST image and the BST frequency distribution of the tumor (Figure 6*B*), the *E·F* image and the *E·F* frequency distribution of the tumor (Figure 6*C*), and curves for *E·F versus* BST (Figure 6*D*). The curves in Figure 6*A* refer to a ~30-pixel-large ROI in the main supplying artery and single pixels in a tumor arteriole, a tumor capillary, and a tumor venule. These curves illustrate the sensitivity of the BST calculations, as the BST values of the pixels in the tumor arteriole, tumor capillary, and tumor venule are given by the time difference between the peaks of the red and black curves, the green and black curves, and the blue and black curves, respectively. A BST value was assigned to each pixel in the vascular mask, giving rise to the BST image and the BST frequency distribution in Figure 6*B*. The BST image showed high BST values in the same tumor regions as the *E·F* image showed low *E·F* values and *vice versa*. There was a significant inverse linear correlation between *E·F* and BST, both when the images were divided into 8 ROIs with a size corresponding to 4 × 4 *E·F* pixels (Figure 6*D*, *left*; R^2 = 0.75; P = .0053) and 32 ROIs with a size corresponding to 2 × 2 *E·F* pixels (Figure 6*D*, *right*; R^2 = 0.35; P = .00037).

Discussion

Comparative examinations of DCE-MRI–derived parametric images and intravital microscopy-derived morphologic and functional images of the microvasculature of tumors have not been reported previously, probably because current window chambers are made of titanium frames with screws and nuts of stainless steel and thus are MR-incompatible. In the work reported here, we present a novel in-house-made MR-compatible window chamber that does not induce artifacts in MR images of tumors growing in the chamber. Thus, high-resolution *E·F* images of the tumors can be produced, and because the chamber was equipped with a plastic window providing excellent visual access to the tissue in the chamber, detailed optical images of the morphology and function of the microvascular network can be provided by using intravital microscopy techniques.

Several studies have indicated that window chamber tumors growing as a thin sheet between two windows may differ physiologically from tumors with a spherical shape growing in the intradermal or

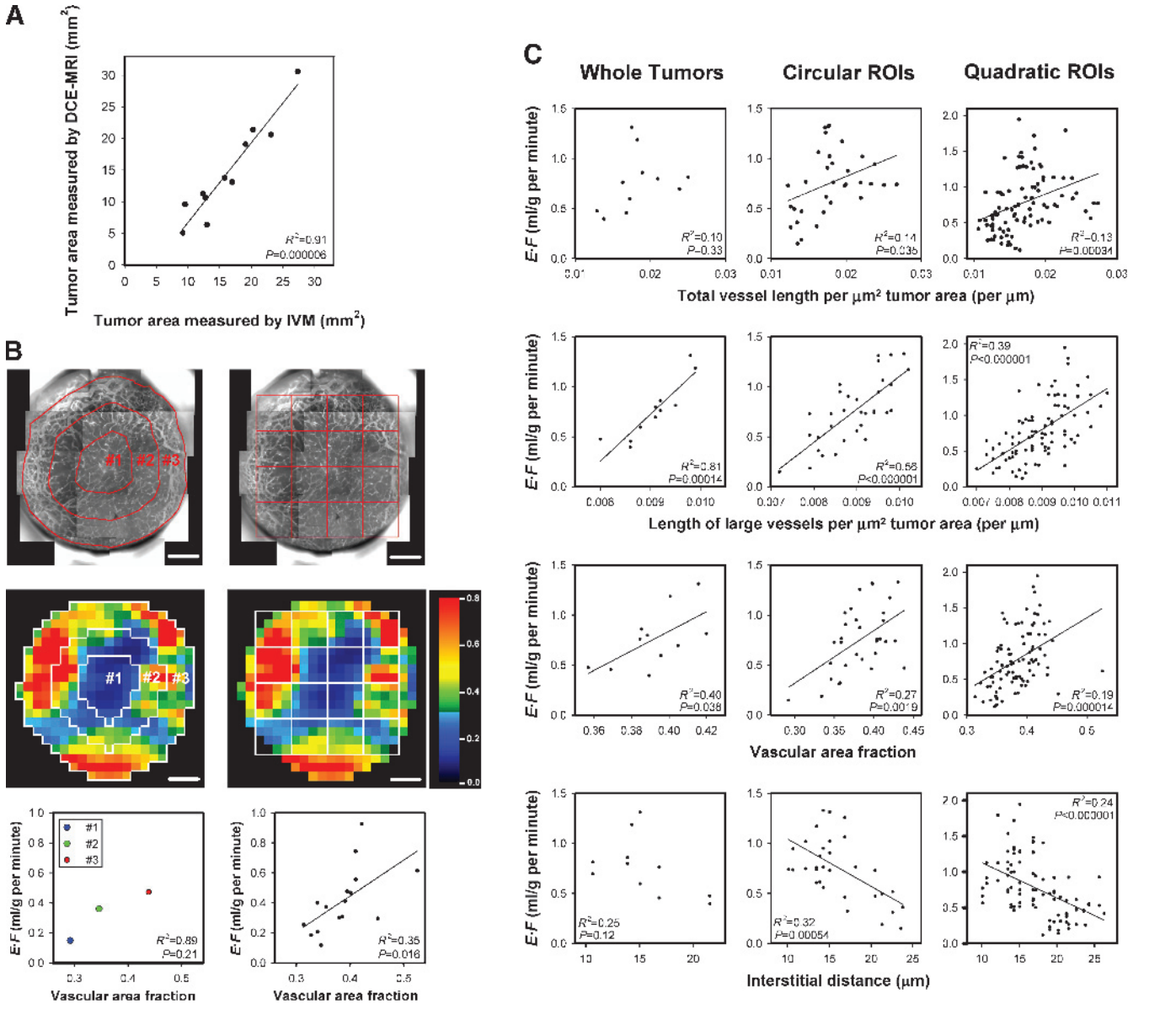

Figure 4. *E·F* derived by DCE-MRI *versus* microvascular density derived by intravital microscopy for eleven A-07-GFP tumors. (A) Tumor area measured by DCE-MRI *versus* tumor area measured by intravital microscopy (IVM). (B) Intravital microscopy images of the microvascular network (upper panels), *E·F* images (middle panels), and plots of *E·F versus* vascular area fraction (lower panels) for a heterogeneous and poorly vascularized tumor. The images illustrate how the tumors were divided into three concentric circular ROIs and quadratic ROIs. The circular ROIs are bounded by lines drawn at distances of $nR/3$ from the tumor center, where R is tumor radius and n is ROI number. The size of the quadratic ROIs corresponds to 4 × 4 *E·F* pixels (i.e., 1.24 × 1.24 mm^2). The *E·F* scale is given by the color bar. Scale bars, 1 mm. The plots show median *E·F versus* vascular area fraction for the three circular ROIs (left panel) and the sixteen quadratic ROIs (right panel). (C) Plots of median *E·F versus* microvascular density. The symbols represent individual tumors (left panels), individual circular ROIs (middle panels), and individual quadratic ROIs (right panels). Peripheral quadratic ROIs consisting of <75% tumor pixels were not included in the analysis. The parameters used for microvascular density are total vessel length per µm^2 tumor area (first row), length of large vessels (i.e., vessels with diameter ≥23.8 µm, corresponding to 7 pixels) per µm^2 tumor area (second row), vascular area fraction [i.e., # pixels (vascular mask)/# pixels (tumor); third row], and interstitial distance (i.e., the median of the distance from a tumor pixel outside the vascular mask to the nearest pixel within the vascular mask; fourth row). Solid lines represent significant correlations and were fitted to the data by linear regression analysis.

subcutaneous space [18–21]. Thus, the interstitial fluid pressure may be higher in two-dimensional window chamber tumors than in three-dimensional subcutaneous tumors because the windows may restrict the flow of interstitial fluid from the tumor tissue to the surrounding normal tissue. To limit the proportions of possible chamber-induced physiological changes in the tumor tissue, the A-07-GFP tumors studied here were grown as a hemisphere in a chamber with a single window, with the plane surface facing the window. When the chamber was removed after an experiment, skin discoloration or tissue swelling was not seen, in contrast to what has been observed for two-window chambers. Moreover, studies in our laboratory of A-07-GFP window chamber tumors similar to those studied here have shown

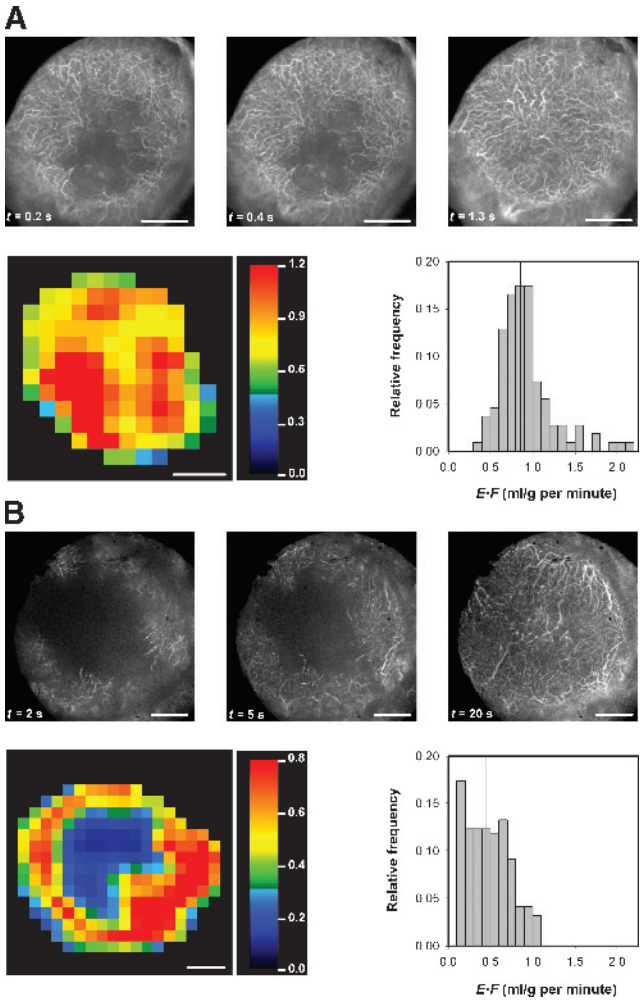

Figure 5. Three single frames from the first-pass imaging movie, the *E·F* image, and the *E·F* frequency distribution of a well-vascularized (A) and a poorly vascularized (B) A-07-GFP tumor. The frames were recorded 0.2, 0.4, and 1.3 seconds (A) and 2, 5, and 20 seconds (B) after the TRITC-dextran bolus had reached the main tumor-supplying artery. The color bars show the *E·F* scales. The vertical lines in the *E·F* frequency distributions indicate median *E·F*. Scale bars, 1 mm.

that (1) the tumors have an interstitial fluid pressure that is similar to that measured in intradermal A-07 tumors and (2) the tumors do not possess hypoxic regions (i.e., regions staining positive for the hypoxia marker pimonidazole cannot be detected in histologic preparations of the tissue) [unpublished data]. Consequently, it is highly unlikely that our chamber induced an artificially high interstitial fluid pressure and hypoxia in the tumor tissue that led to hypoxia-induced secretion of proangiogenic factors, elevated angiogenic activity, and increased blood perfusion.

Different strategies are being used for deriving relevant kinetic parameters from DCE-MRI series [6]. The principal approaches make use of pharmacokinetic models, assuming that the transvascular flux of contrast agent is limited purely by blood flow, purely by vessel permeability, or by both blood flow and vessel permeability. The Kety model assumes that the uptake of Gd-DTPA in tissues is governed primarily by the blood perfusion. It is highly probable that this assumption is valid for the A-07-GFP tumors examined here, as several independent studies suggest that the transvascular flux of Gd-DTPA in A-07 tumors is not limited by the permeability of the microvessel wall. Thus, electron microscopy examinations have shown that the microvasculature of A-07 tumors has severe structural abnormalities, including high frequency of endothelial fenestrae and large interendothelial gaps, incomplete endothelial lining, and discontinuous basement membrane, and thus should be highly permeable to low-molecular-weight hydrophilic contrast agents such as Gd-DTPA

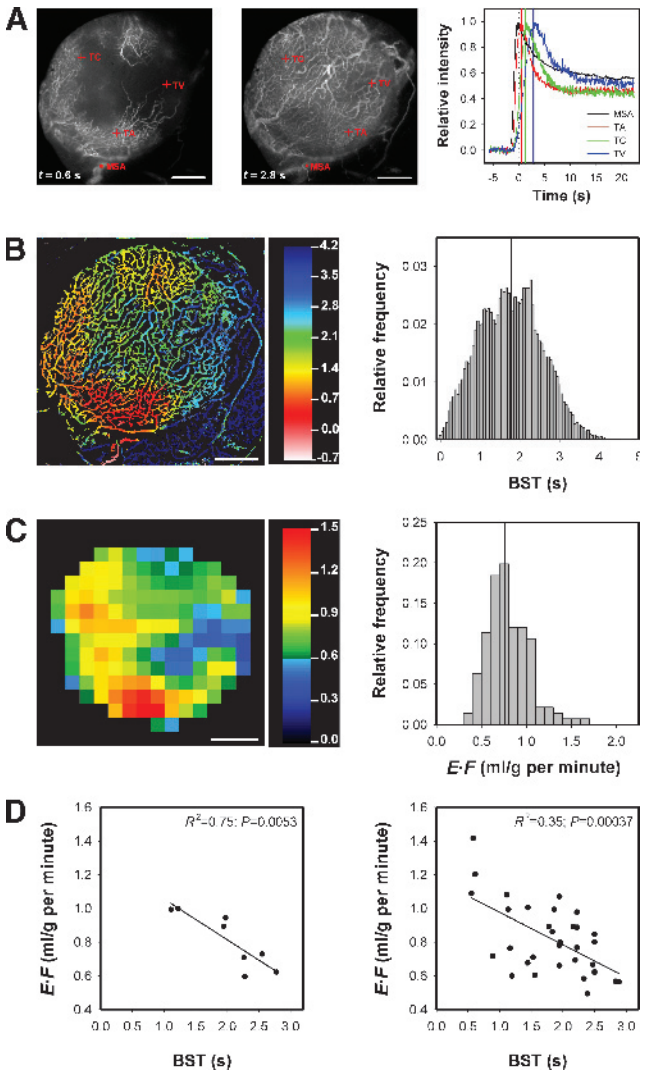

Figure 6. The figure refers to a heterogeneously vascularized A-07-GFP tumor and shows two single frames from the first-pass imaging movie, recorded 0.6 and 2.8 seconds after the bolus had reached the main tumor-supplying artery, and curves for relative signal intensity *versus* time for the ROIs indicated in the frames (A), the BST image and the BST frequency distribution (B), the *E·F* image and the *E·F* frequency distribution (C), and plots of *E·F versus* BST (D). The ROIs and curves in (A) refer to the main supplying artery (MSA), a tumor arteriole (TA), a tumor capillary (TC), and a tumor venule (TV). The scales of the BST and *E·F* images are given by the color bars. The vertical lines in the BST and *E·F* frequency distributions indicate median BST and median *E·F*. Scale bars, 1 mm. The plots show median *E·F versus* median BST for quadratic ROIs with a size corresponding to 4 × 4 (left panel) or 2 × 2 (right panel) *E·F* pixels (i.e., 1.24 × 1.24 and 0.62 × 0.62 mm^2, respectively). The symbols represent individual ROIs. The solid lines represent curves fitted to the data by linear regression analysis.

[24]. Bioscope imaging studies have demonstrated that the intratumor heterogeneity in the uptake of freely diffusible radioactive blood flow tracers is similar to that of Gd-DTPA in A-07 tumors, suggesting that the E for Gd-DTPA is uniformly close to unity [31]. Moreover, DCE-MRI measurements have revealed that the effective microvascular permeability constants for macromolecules and 20-nm-diameter superparamagnetic iron oxide particles are extremely high in A-07 tumors [32,33].

The most commonly used pharmacokinetic model for analyzing DCE-MRI data of tumors is the model known as the generalized kinetic model of Tofts [6]. This model is the model of choice when studying tumors with low, unknown, or heterogeneous microvascular permeability for Gd-DTPA. The parameters of the Kety model ($E{\cdot}F$ and λ) are related to the parameters of the Tofts model [K^{trans} (the volume transfer constant of Gd-DTPA) and v_e (the distribution volume of Gd-DTPA per unit volume of tissue)] by the following expressions: $E{\cdot}F = K^{trans}/[\rho \cdot (1 - Hct)]$ and $\lambda = v_e/[\rho \cdot (1 - Hct)]$, where ρ is the density of the tissue and Hct is the hematocrit. In the present communication, we chose to use the Kety formulation, primarily because $E{\cdot}F$ is preferable to K^{trans} as a parameter for tumor vascularity in tumors where the uptake of Gd-DTPA is known to be limited purely by the blood flow. K^{trans} has a per-minute unit and is simply a rate constant with no direct physical or physiological meaning. Conversely, the unit of $E{\cdot}F$ is ml/g per minute, implying that numerical values of $E{\cdot}F$ can be compared directly with numerical values of tumor blood perfusion. In an earlier study of 200- to 700-mm^3 intradermal A-07 tumors, median $E{\cdot}F$ was found to range from 0.05 to 0.39 ml/g per minute with a mean value of 0.20 ml/g per minute [17]. Interestingly, these values are similar to those achieved when tumor blood perfusion was measured with invasive methods in intradermal A-07 tumors [34]. Median $E{\cdot}F$ of the tumors studied here ranged from 0.40 to 1.31 ml/g per minute with a mean value of 0.76 ml/g per minute and was thus higher than those mentioned above, most likely because the window chamber tumors studied here were substantially smaller than the intradermal tumors studied earlier. This suggestion is consistent with the observation that intradermal A-07 tumors with volume >200 mm^3 have a mean fraction of radiobiologically hypoxic cells of 5% to 10% [16,35], whereas radiobiologically hypoxic cells cannot be detected in intradermal A-07 tumor with volume <200 mm^3 [36].

The DCE-MRI was performed by using a voxel size of 0.31 × 0.31 × 2.0 mm^3 and a time resolution of 14 seconds. Previous studies in our laboratory of intradermal A-07 tumors have shown that the signal-to-noise ratio at this voxel size is sufficiently high to provide well-defined Gd-DTPA concentration *versus* time curves and that the initial rising part of the Kety curves is determined precisely at this time resolution [14,16,17,30]. These observations were confirmed in the present study of A-07-GFP window chamber tumors.

Adequate evaluation of the usefulness of DCE-MRI in characterizing the vascularity of tumors requires comparisons of DCE-MRI–derived parameters with morphologic as well as functional parameters of the microvascular network. Several morphologic and functional parameters are being used for describing the microvascular network of tumors growing in window chambers [18–21]. In the work reported here, microvascular density, measured as total vessel length per μm^2 tumor area, length of large vessels per μm^2 tumor area, vascular area fraction, and interstitial distance, was used as morphologic parameter, and BST was used as functional parameter. By using these parameters, it was possible to characterize the morphology and function of the microvascular network of the tumors in a single experiment, and most importantly, our strategy made it possible to compare DCE-MRI–derived parametric images with morphologic and functional microvascular images of whole tumors.

The calculation of microvascular density and the computation of BST images required production of vascular masks. As demonstrated in Figure 3, our algorithms produced vascular masks of high quality (i.e., small vessels were detected as well as large vessels, and the diameter of the vessels was retained in the masks). A weakness of our approach is, however, that the vascular masks represented two-dimensional projections of the three-dimensional tumor vasculature. Calculation of microvascular density from two-dimensional vascular masks results in an overestimation of the microvascular density because of contributions from out-of-plane vasculature. The magnitude of the overestimation may depend on the parameter used for microvascular density, and consequently, four different parameters were used for microvascular density in the present work. However, when comparing DCE-MRI–derived parametric images with intravital microscopy-derived images of tumor vascularity, high depth resolution of the intravital microscopy images is not crucial because MR scans also have a substantial thickness (2 mm in the study reported here).

The function of the tumor microvascular networks was assessed by measuring BST. Previous work has shown that this parameter can be measured with high accuracy in any pixel within the vascular network of tumors growing in ~250-μm-thick window chamber preparations and that a time resolution of 55.6 milliseconds (18 fps) is sufficient to demonstrate that BST increases gradually along individual vessel segments in the tumor tissue [23]. In the present work, we demonstrate that BST can be assessed with similar accuracy also in many hemispherical window chamber tumors, as illustrated in Figure 6. The calculation of high-quality BST images requires that the great majority of the pixels within the vascular mask show fluorescence intensity *versus* time curves with a well-defined peak (cf., Figure 6*A*, *right panel*). However, this requirement was not fulfilled in all hemispherical tumors studied here. Some tumors, particularly large tumors with highly irregular microvascular networks, showed regions with very delayed blood supply (i.e., regions that were not reached by the TRITC-dextran bolus until after a lag time of up to 20 seconds), as illustrated in Figure 5*B*. The peak of the fluorescence intensity *versus* time curves in these regions was poorly defined, and consequently, it was not possible to produce high-quality BST images and frequency distributions. For these tumors, only rough estimates of the BST values could be produced from the delay in contrast appearance.

If $E{\cdot}F$ is going to be a clinically useful parameter for noninvasive characterization of the vascularity of tumors, images of $E{\cdot}F$ have to reflect morphologic and functional images of the tumor microvasculature. Ideally, significant correlations between $E{\cdot}F$ and microvascular parameters should exist within heterogeneous tumors as well as across individual tumors, both for whole tumors and tumor subregions. Our study showed unequivocally that $E{\cdot}F$ images mirror morphologic and functional images of the microvasculature of A-07-GFP tumors well. Thus, strong correlations were found between $E{\cdot}F$ and microvascular density, both for whole tumors and tumor subregions, regardless of whether microvascular density was measured as total vessel length per μm^2 tumor area, length of large vessels per μm^2 tumor area, vascular area fraction, or interstitial distance. Interestingly, $E{\cdot}F$ showed the strongest correlation with the density of large-diameter vessels, possibly because tumor blood perfusion is influenced strongly by these vessels. Moreover, $E{\cdot}F$

was found to reflect the intratumor and intertumor heterogeneity in BST. Thus, tumors showing high and homogeneous *E·F* values showed low and homogeneous BST values. In heterogeneous tumors, regions showing high *E·F* values colocalized with regions showing low BST values and regions showing low *E·F* values colocalized with regions showing high BST values, regardless of whether BST was assessed accurately or just estimated from the delay in contrast appearance.

In conclusion, the work reported here strongly suggests that parametric images providing information on the morphology and function of the microvasculature of tumors can be obtained by Gd-DTPA–based DCE-MRI. The possibility that DCE-MRI may be developed to be a useful noninvasive diagnostic method for characterizing the microvasculature of human tumors merits clinical investigation.

Acknowledgments

We thank Jørn Iversen at the Norwegian Radium Hospital for producing the MR-compatible window chamber and Lars Aurdal at the Norwegian Computing Centre for software development.

References

[1] Vaupel P, Kallinowski F, and Okunieff P (1989). Blood flow, oxygen and nutrient supply, and metabolic microenvironment of human tumors: a review. *Cancer Res* **49**, 6449–6465.

[2] Brown JM and Giaccia AJ (1998). The unique physiology of solid tumors: opportunities (and problems) for cancer therapy. *Cancer Res* **58**, 1408–1416.

[3] Rofstad EK (2000). Microenvironment-induced cancer metastasis. *Int J Radiat Biol* **76**, 589–605.

[4] Vaupel P (2004). Tumor microenvironmental physiology and its implications for radiation oncology. *Semin Radiat Oncol* **14**, 198–206.

[5] Tofts PS (1997). Modeling tracer kinetics in dynamic Gd-DTPA MR imaging. *J Magn Reson Imaging* **7**, 91–101.

[6] Tofts PS, Brix G, Buckley DL, Evelhoch JL, Henderson E, Knopp MV, Larsson HBW, Lee T-Y, Mayr NA, Parker GJM, et al. (1999). Estimating kinetic parameters from dynamic contrast-enhanced T_1-weighted MRI of a diffusable tracer: standardized quantities and symbols. *J Magn Reson Imaging* **10**, 223–232.

[7] Padhani AR (2002). Dynamic contrast-enhanced MRI in clinical oncology: current status and future directions. *J Magn Reson Imaging* **16**, 407–422.

[8] Buckley DL, Drew PJ, Mussurakis S, Monson JR, and Horsman A (1997). Microvessel density of invasive breast cancer assessed by dynamic Gd-DTPA–enhanced MRI. *J Magn Reson Imaging* **7**, 461–464.

[9] Hawighorst H, Weikel W, Knapstein PG, Knopp MV, Zuna I, Schönberg SO, Vaupel P, and van Kaick G (1998). Angiogenic activity of cervical carcinoma: assessment by functional magnetic resonance imaging–based parameters and a histomorphological approach in correlation with disease outcome. *Clin Cancer Res* **4**, 2305–2312.

[10] Tynninen O, Aronen HJ, Ruhala M, Paetau A, von Boguslawski K, Salonen O, Jääskeläinen J, and Paavonen T (1999). MRI enhancement and microvascular density in gliomas. Correlation with tumor cell proliferation. *Invest Radiol* **34**, 427–434.

[11] Su MY, Cheung YC, Fruehauf JP, Yu H, Nalcioglu O, Mechetner E, Kyshtoobayeva A, Chen SC, Hsueh S, McLaren CE, et al. (2003). Correlation of dynamic contrast enhancement MRI parameters with microvessel density and VEGF for assessment of angiogenesis in breast cancer. *J Magn Reson Imaging* **18**, 467–477.

[12] Matsubayashi R, Matsuo Y, Edakuni G, Satoh T, Tokunaga O, and Kudo S (2000). Breast masses with peripheral rim enhancement on dynamic contrast-enhanced MR images: correlation of MR findings with histologic features and expression of growth factors. *Radiology* **217**, 841–848.

[13] George ML, Dzik-Jurasz AS, Padhani AR, Brown G, Tait DM, Eccles SA, and Swift RI (2001). Non-invasive methods of assessing angiogenesis and their value in predicting response to treatment in colorectal cancer. *Br J Surg* **88**, 1628–1636.

[14] Benjaminsen IC, Graff BA, Brurberg KG, and Rofstad EK (2004). Assessment of tumor blood perfusion by high-resolution dynamic contrast-enhanced MRI: a preclinical study of human melanoma xenografts. *Magn Reson Med* **52**, 269–276.

[15] Benjaminsen IC, Brurberg KG, Ruud EBM, and Rofstad EK (2008). Assessment of extravascular extracellular space fraction in human melanoma xenografts by DCE-MRI and kinetic modeling. *Magn Reson Imaging* **26**, 160–170.

[16] Egeland TA, Gaustad JV, Vestvik IK, Benjaminsen IC, Mathiesen B, and Rofstad EK (2006). Assessment of fraction of radiobiologically hypoxic cells in human melanoma xenografts by dynamic contrast-enhanced MRI. *Magn Reson Med* **55**, 874–882.

[17] Vestvik IK, Egeland TA, Gaustad JV, Mathiesen B, and Rofstad EK (2007). Assessment of microvascular density, extracellular volume fraction, and radiobiological hypoxia in human melanoma xenografts by dynamic contrast-enhanced MRI. *J Magn Reson Imaging* **26**, 1033–1042.

[18] Vajkoczy P, Ullrich A, and Menger MD (2000). Intravital fluorescence videomicroscopy to study tumor angiogenesis and microcirculation. *Neoplasia* **2**, 53–61.

[19] Dewhirst MW, Shan S, Cao Y, Moeller B, Yuan F, and Li CY (2002). Intravital fluorescence facilitates measurement of multiple physiologic functions and gene expression in tumors of live animals. *Dis Markers* **18**, 293–311.

[20] Jain RK, Munn LL, and Fukumura D (2002). Dissecting tumour pathophysiology using intravital microscopy. *Nat Rev Cancer* **2**, 266–276.

[21] Tozer GM, Ameer-Beg SM, Baker J, Barber PR, Hill SA, Hodgkiss RJ, Locke R, Prise VE, Wilson I, and Vojnovic B (2005). Intravital imaging of tumour vascular networks using multi-photon fluorescence microscopy. *Adv Drug Deliv Rev* **57**, 135–152.

[22] Dewhirst MW (1998). Concepts of oxygen transport at the microcirculatory level. *Semin Radiat Oncol* **8**, 143–150.

[23] Øye KS, Gulati G, Graff BA, Gaustad JV, Brurberg KG, and Rofstad EK (2008). A novel method for mapping the heterogeneity in blood supply to normal and malignant tissues in the mouse dorsal window chamber. *Microvasc Res* **75**, 179–187.

[24] Rofstad EK (1994). Orthotopic human melanoma xenograft model systems for studies of tumour angiogenesis, pathophysiology, treatment sensitivity and metastatic pattern. *Br J Cancer* **70**, 804–812.

[25] Rofstad EK, Wahl A, Davies CL, and Brustad T (1986). Growth characteristics of human melanoma multicellular spheroids in liquid-overlay culture: comparisons with the parent tumour xenografts. *Cell Tissue Kinet* **19**, 205–216.

[26] Papenfuss HD, Gross JF, Intaglietta M, and Treese FA (1979). A transparent access chamber for the rat dorsal skin fold. *Microvasc Res* **18**, 311–318.

[27] Rofstad EK, Steinsland E, Kaalhus O, Chang YB, Høvik B, and Lyng H (1994). Magnetic resonance imaging of human melanoma xenografts *in vivo*: proton spin–lattice and spin–spin relaxation times *versus* fractional tumour water content and fraction of necrotic tumour tissue. *Int J Radiat Biol* **65**, 387–401.

[28] Hittmair K, Gomiscek G, Langenberger K, Recht M, Imhof H, and Kramer J (1994). Method for the quantitative assessment of contrast agent uptake in dynamic contrast-enhanced MRI. *Magn Reson Med* **31**, 567–571.

[29] Kety S (1960). Theory of blood–tissue exchange and its application to measurements of blood flow. *Methods Med Res* **8**, 228–236.

[30] Brurberg KG, Benjaminsen IC, Dørum LMR, and Rofstad EK (2007). Fluctuations in tumor blood perfusion assessed by dynamic contrast-enhanced MRI. *Magn Reson Med* **58**, 473–481.

[31] Graff BA, Benjaminsen IC, Brurberg KG, Ruud EBM, and Rofstad EK (2005). Comparison of tumor blood perfusion assessed by dynamic contrast-enhanced MRI with tumor blood supply assessed by invasive imaging. *J Magn Reson Imaging* **21**, 272–281.

[32] Bjørnæs I and Rofstad EK (2001). Microvascular permeability to macromolecules in human melanoma xenografts assessed by contrast-enhanced MRI—intertumor and intratumor heterogeneity. *Magn Reson Imaging* **19**, 723–730.

[33] Graff BA, Vangberg L, and Rofstad EK (2004). Quantitative assessment of uptake and distribution of iron oxide particles (NC 100150) in human melanoma xenografts by contrast-enhanced MRI. *Magn Reson Med* **51**, 727–735.

[34] Lyng H, Dahle GA, Kaalhus O, Skretting A, and Rofstad EK (1998). Measurement of perfusion rate in human melanoma xenografts by contrast-enhanced magnetic resonance imaging. *Magn Reson Med* **40**, 89–98.

[35] Rofstad EK and Måseide K (1999). Radiobiological and immunohistochemical assessment of hypoxia in human melanoma xenografts: acute and chronic hypoxia in individual tumours. *Int J Radiat Biol* **75**, 1377–1393.

[36] Rofstad EK, Tunheim SH, Mathiesen B, Graff BA, Halsør EF, Nilsen K, and Galappathi K (2002). Pulmonary and lymph node metastasis is associated with primary tumor interstitial fluid pressure in human melanoma xenografts. *Cancer Res* **62**, 661–664.